

Supporting Information

Imaging on-surface hierarchical assembly of chiral supramolecular networks

Laerte L. Patera,^{*a,b,c} Zhiyu Zou,^{a,d} Carlo Dri,^{a,c,e} Cristina Africh,^a Jascha Repp,^b and Giovanni Comelli^{a,c}

a) IOM-CNR Laboratorio TASC, Area Science Park, 34149 Trieste, Italy

b) Institute of Experimental and Applied Physics, University of Regensburg, 93053 Regensburg, Germany D

c) Department of Physics, University of Trieste, 34127 Trieste, Italy

d) Abdus Salam International Centre for Theoretical Physics, 34151 Trieste, Italy

e) Elettra - Sincrotrone Trieste S.C.p.A., 34149 Trieste, Italy

*Corresponding author: laerte.patera@ur.de

Contents:

1. Chain structure
2. Chiral defects
3. Chain orientation
4. Integrated Residence Time analysis

1. Chain structure

In Fig. S11, (properly scaled) structural models are superimposed to the AFM image shown in Fig. 2b. Fig. S11a shows the model reported in Fig. 2c, where intermolecular bonding occurs through aryl-aryl interaction mediated by coordinating Cu adatoms. Instead, in Fig. S11b the molecular models have the anthracene long axis parallel to the chain direction. It is possible to observe that for the model in Fig. S11a, the protruding C-H bonds fit well the positions of the main bright features in the experimental image (indicated by red arrows). Conversely, in the model in Fig. S11b there is not a good match between the molecular structure and the details of the AFM image.

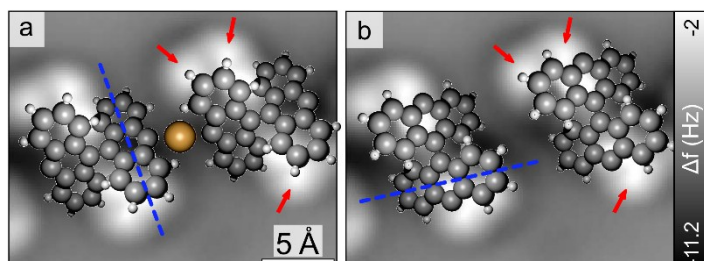


Fig. S11 3D models of the possible molecular structures superimposed to the nc-AFM image of a dimer obtained with a CO tip [$\Delta z = 2.9 \text{ \AA}$, 6.8 K, STM setpoint: 1 V, 1.4 pA]. The arrows specified the main bright (repulsive) features. Blue lines indicate the long-axis direction of the anthracene units.

2. Chiral defects

Here, we consider the defective structures and their formation pathways. Despite the molecular islands commonly appearing as composed of only one enantiomer (see Fig. 2a), it is possible to observe defects inside the islands (indicated by arrows in Fig. S12a). The nature of these structures has been clarified through nc-AFM images with a CO-functionalized tip.¹ Fig. S12b shows two coupled chains, with a defect in the top-left corner. In Fig. S12c, superimposed stick-and-ball models indicate the molecule orientations inside the complex, allowing for the identification of the defect as a radical of the opposite chirality (chiral defect).

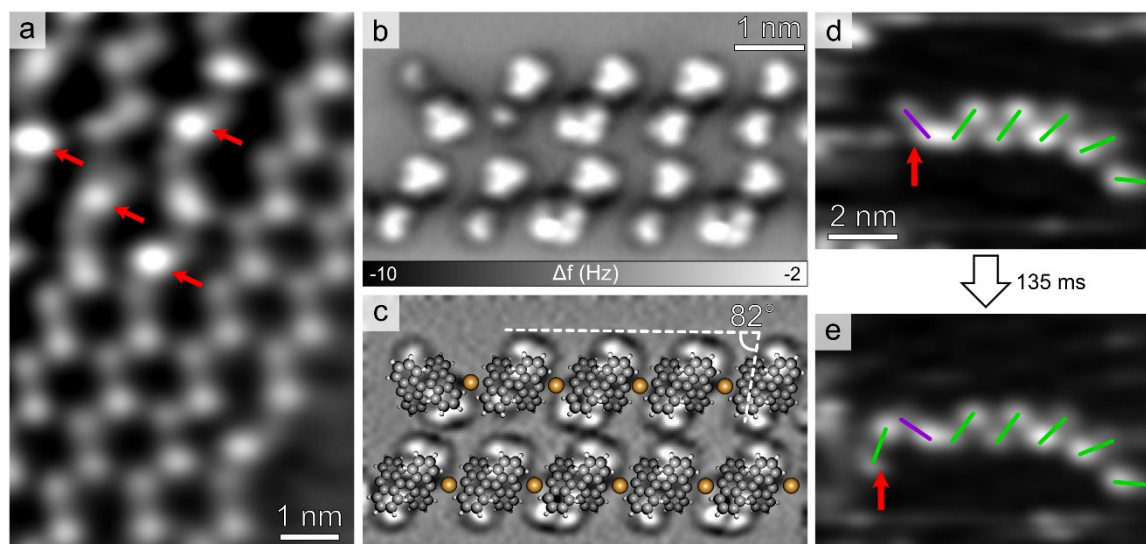


Fig. S12 Chiral defect structures and formation pathway. (a) STM image of a molecular island [-1 V, 1.4 nA, 294 K, 27 ms/ frame]. Red arrows indicate defects. (b) nc-AFM image of a double chain obtained with a CO tip [$\Delta z = 1.6 \text{ \AA}$, 6.8 K, STM setpoint: 1 V, 1.4 pA]. A chiral defect is present in the top-left corner. (c) 2nd order high-pass filtered image of (b), with superimposed models of the dehalogenated radicals and of the Cu adatoms. The angle between the azimuthal orientation of anthracene long axis and chain direction is indicated by dashed lines. (d-e) Selected STM frames showing heterochiral attachment to a chain termination [-1 V, 1.4 nA, 294 K, 27 ms/ frame].

In principle, chiral defects can form during the organometallic coordination,² or due to conformational switching.³ The latter mechanism has been reported, for example, by Weigert et al.³, where prochiral molecules deposited on Au(111) spontaneously undergo conformational changes upon end-group rotation along a C-C bond. In contrast, in our system, acquiring extended STM time-series on defective regions, we never observed a chirality-switching event, even though the

substrate temperature was increased to 370 K. However, it has to be noted that the different molecule-substrate interaction could play an important role in increasing the kinetic barriers for the switching.

Once ruled out conformation switching as a source of defect formation, we investigated the attachment of single radicals, addressing the enantioselectivity of the processes. While only homochiral coupling events are observed for the case of radical attachment to 2D island edges (see Fig. 3c-d), STM time-series reveal a small probability for a single radical to attach to a chain of the opposite chirality, as shown in Fig. SI2d-e. In the first frame (Fig. SI2d), a β chain with an α radical on the left side is present at the centre of the image, then, after 135 ms (Fig. SI2e), an additional β radical attaches to the α one, giving rise to another heterochiral organometallic coordination. In this way, we unambiguously determined the mechanism responsible for chiral defect formation, revealing the lack of enantiospecificity of the organometallic bond.

Despite the fact that the high enantioselectivity of interchain coupling has been identified as the driving force for chirality expression in 2D assemblies, chiral defects are sometimes found in large islands (see Fig. SI2a). This observation reveals that, for the case of long organometallic chains, the presence of single defects cannot completely prevent aggregation of achiral chains.

Chain orientations

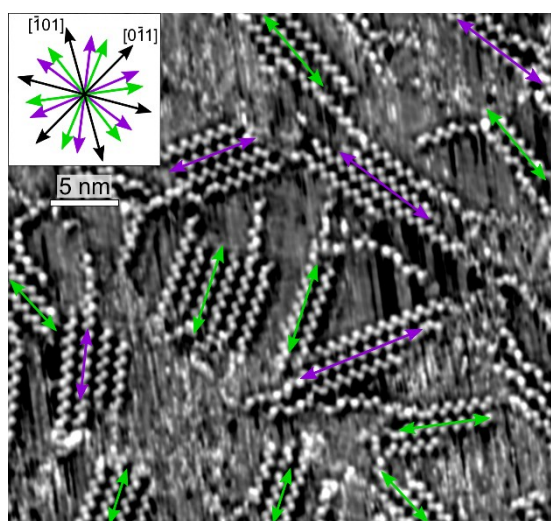


Fig. SI3 STM image of molecular chains and islands on Cu(111) [-1 V, 0.5 nA, 295 K, 60 s/ frame]. Inset: possible chain orientations are highlighted with coloured arrows, according to the molecular chirality. Cu crystallographic directions are indicated in black.

In Fig. SI3, it is possible to observe only six different chain directions (three for α and three for β domains). The angles between the chain orientation are in agreement with the previous results reported by Han et al.⁴ The observed orientations corresponding to the different molecular chiralities are distributed symmetrically with respect to the Cu crystallographic direction (indicated in red).⁵

3. Integrated Residence Time analysis

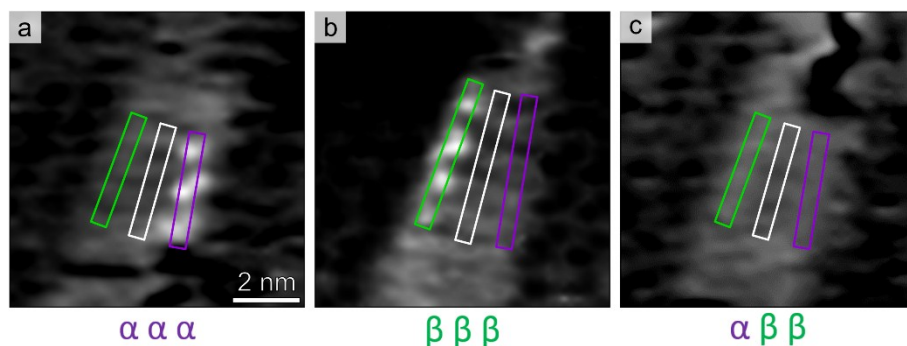


Fig. SI4 (a-c) IRT maps extracted from 36 consecutive frames (≈ 1 s) for the case of: $\alpha\alpha\alpha$, $\beta\beta\beta$ and $\alpha\beta\beta$ chains, respectively. Rectangles indicate the integration regions for each chain configuration.

For the extraction of IRT maps shown in Fig. 5(b-d-f), 36 consecutive frames were first averaged, then a background image has been subtracted. The background image was chosen from the frames where the trimer chain was not present between

the chiral edges, having diffused temporarily away. From the images in Fig. S14, we extracted the parameter S , which expresses the difference between average residence times along the two edges with opposite chirality facing the trench:

$$S = \frac{I_{\alpha} - I_{\beta}}{I_{\alpha} + I_{\beta}},$$

where I_{α} and I_{β} are the integrated pixel intensities calculated along the island edges with respect to the background level, evaluated in the middle of the trench (see white rectangle in Fig. S14). Since the β edge is one molecular unit longer than the α one (see Fig. 5a), while the α chain has only one stable homochiral configuration, the β one has two different stable adsorption positions along the edge. For this reason, in Fig. S14b, a larger integration region has been chosen.

Due to the lower coordination stability in the interchain coupling respect to the organometallic coordination, the former exhibits a notably higher formation/disruption rate with respect to the latter. This allowed us to observe a large number of events, giving rise to a reasonable statistic, necessary for the quantitative analysis of the IRT. For the case of the organometallic coordination, the average event rate at the equilibrium was found to be lower than one per minute, thereby hindering a statistical analysis.

STM movies

Three STM movies are available online:

Movie1, $\alpha\alpha\alpha$ chain [-1 V, 1.4 nA, 294 K, 27 ms/ frame]

Movie2, $\beta\beta\beta$ chain [-1 V, 1.4 nA, 294 K, 27 ms/ frame]

Movie3, $\alpha\beta\beta$ chain [-1 V, 1.4 nA, 294 K, 27 ms/ frame]

References

- 1 L. Gross, F. Mohn, N. Moll, P. Liljeroth and G. Meyer, *Science*, 2009, **325**, 1110–1114.
- 2 D. Heim, D. Ćija, K. Seufert, W. Auwarter, C. Aurisicchio, C. Fabbro, D. Bonifazi and J. V. Barth, *J. Am. Chem. Soc.*, 2010, **132**, 6783–6790.
- 3 S. Weigelt, C. Busse, L. Petersen, E. Rauls, B. Hammer, K. V Gothelf, F. Besenbacher and T. R. Linderoth, *Nat. Mater.*, 2006, **5**, 112–117.
- 4 P. Han, K. Akagi, F. F. Canova, H. Mutoh, S. Shiraki, K. Iwaya, P. S. Weiss, N. Asao and T. Hitosugi, *ACS Nano*, 2014, **8**, 9181–9187.
- 5 Q. Chen and N. V. Richardson, *Nat. Mater.*, 2003, **2**, 324–328.